AIAA JOURNAL
Vol. 46, No. 9, September 2008

Propulsive Efficiency of a Moving Airfoil at Transitional Low Reynolds Numbers

Jan Windte* and Rolf Radespiel†
Technical University of Braunschweig, 38106 Braunschweig, Germany

DOI: 10.2514/1.30569

Unsteady Reynolds-averaged Navier–Stokes simulations of the low-Reynolds-number flow past an SD7003 airfoil with combined plunge and pitch motion at $Re = 60,000$ are presented in which transition takes place across laminar separation bubbles. The numerical simulation approach includes transition prediction that is based on linear stability analysis applied to unsteady mean flow data. A parameter study for three reduced frequencies of $k = 0.25$, 0.5, and 1.0 is conducted. The drag losses encountered are quantified by a comparison with results using inviscid unsteady airfoil theory. High propulsive efficiencies are gained within the investigated thrust range, which goes to about 10 times the steady onflow airfoil drag.

Nomenclature

A	=	amplitude of oscillation
c	=	airfoil chord
c_{df}	=	friction drag coefficient
c_{dp}	=	pressure drag coefficient
c_l	=	lift coefficient
c_T^*	=	thrust coefficient
c_x, c_y	=	force coefficients in the coordinate system aligned to the freestream direction
$c_{x,\mathrm{stat}}$	=	drag coefficient for stationary onflow
c_π	=	power coefficient
f	=	frequency of airfoil motion
k	=	reduced frequency of airfoil motion
M_y	=	moment around the y axis
N	=	N factor
N_{crit}	=	critical N factor
n	=	amplitude exponent of the single wave mode
P	=	power
p	=	pressure
T	=	period length
Tu	=	turbulence intensity
t	=	time
U_∞	=	freestream velocity
u, v, w	=	velocity components
v_g	=	group velocity of the single wave mode
x, y, z	=	local Cartesian coordinates of stability analysis in the streamwise, spanwise, and normal directions
z_1/c	=	plunging amplitude
α	=	complex wave number in the x direction, angle of attack
α_0	=	stationary/mean angle of attack
α_1	=	pitching amplitude
α_{eff}	=	effective angle of attack
$\Delta\alpha_{\mathrm{eff}}$	=	effective angle-of-attack amplitude
β	=	complex wave number in the y direction
ζ	=	angle of attack from plunge motion
η_P	=	propulsive efficiency
κ	=	ratio of specific heats
λ	=	ratio of pitch and plunge amplitude
ρ	=	density
$\rho\overline{u'v'}$	=	turbulent shear stress
φ	=	phase shift between pitch and plunge motion
ω	=	complex frequency of wave mode

Subscript

L	=	large amplitudes

Superscript

$\bar{\ }$	=	time averages

I. Introduction

ADVANCES in the field of microsystem technologies enable the development of micro aerial vehicles (MAVs) with a broad variety of applications. Some of the MAV concepts consider flapping-wing propulsion because of the potentially high propulsive efficiency and the capability of hovering flight. Extensive development is taking place on birdlike flapping-wing machines, resulting in constructions with masses from about 1 kg down to a few grams‡ [1–3]. A few designs even exist that do not mimic the flapping of birds but use pitching and plunging wings in tandem and biplane configurations [4,5].

For all configurations, the motion forms of the 2D airfoil sections play an important role. Many parameter studies have already been performed on moving airfoils numerically [6–12] as well as experimentally [4,10,13]. In almost all studies, only a single parameter (plunge amplitude, pitch amplitude, phase shift, or frequency) is changed at one time. Very often the frequency is varied, because it correlates to the speed of the propulsion engine and might be the easiest way to control thrust. However, from an aerodynamic point of view, it makes more sense to vary multiple parameters simultaneously to obtain high propulsive efficiencies. Küssner's [14] inviscid unsteady airfoil theory gives a constant propulsive efficiency for a constant ratio between the pitch and plunge amplitudes and a constant frequency, independent of the amount of thrust produced. One objective of this study is to verify if this also holds true for the viscous case.

Most viscous flow calculations of moving airfoils performed thus far assume either purely laminar or fully turbulent flow. In the present study, transitional flow is simulated, including laminar separation bubbles (LSBs) that are usually involved in the transition process. LSBs can create additional pressure drag as they displace the outer inviscid flow. A more dramatic effect occurs if the transition process

Received 20 February 2007; revision received 9 October 2007; accepted for publication 5 November 2007.

*Research Scientist, Institute of Fluid Mechanics; j.windte@tu-braunschweig.de.

†Professor, Head, Institute of Fluid Mechanics; r.radespiel@tu-braunschweig.de. Senior Member AIAA.

‡Data available online at www.ornithopter.org/projects.shtml [retrieved 2008].

in the separated shear layer is relatively slow and the adverse pressure gradient is strong. Then turbulent momentum transport is not sufficient to close the bubble and a large separation occurs that extends right to the trailing edge. This causes a sudden loss of lift and a strong increase of drag, along with significant hysteresis effects of force coefficients with varying angle of attack. For the low-disturbance environment investigated in this paper, according to the research of Würz [15], Lang et al. [16], and Marxen et al. [17], the primary instability mechanism of LSBs is initially of the Tollmien–Schlichting (TS) type and remains dominated by this type up into the separated-flow region. There, a smooth shift over to the Kelvin–Helmholtz (KH) instability may take place [18]. These findings motivate the use of the e^N method for transition prediction of airfoils with LSBs at low Reynolds numbers. We solve the unsteady Reynolds-averaged Navier–Stokes equations (URANS) and therefore use a recent extension of the e^N method for unsteady flows [19]. The present paper presents numerical flow simulations based on this approach for the SD7003 airfoil using a systematic variation of pitch and plunge motion parameters. These results indicate that physically based transition modeling is needed in engineering the design of flapping-wing propulsion. The SD7003 airfoil was chosen not only because it is known to perform well at low Reynolds numbers and steady incoming flow, but also because it has been established as a standard airfoil in the low-Reynolds-number community with many experimental and numerical results available [20]. No effort was put into unsteady airfoil optimization; thus, other airfoils might be better suited for the unsteady flows investigated.

II. Numerical Simulation Methods

The present numerical simulation approach is based on URANS solutions coupled with a sound transition-prediction method. Details of the development of this approach and its validation were recently published [19]. Only a brief overview is given here, supplemented by a few details on the code-execution procedures.

A. Simulation Approach

The simulation approach addresses the computation of low-Reynolds number flows with laminar separation bubbles using the unsteady Reynolds-averaged Navier–Stokes equations. The transition location along the airfoil is estimated by using the results of stability analysis, which is performed by directly investigating the velocity profiles from the RANS solution with a solver for the linear stability equations (LST). Waves due to viscous (TS) or inviscid (KH) instability mechanism are covered by the stability analysis [18]. The amplification rates of the primary instabilities in this stage computed by LST compare to the rates predicted by well-resolved direct numerical simulation [18], almost within plotting accuracy. Using the simulation-approach method [21], the calculated amplification rates are used to predict the transition location by comparison with a critical N factor.

B. Navier–Stokes Code FLOWer

The Navier–Stokes solver FLOWer [22] uses a block-structured computational domain around the aerodynamic configuration. The flow equations are discretized based on the finite volume approach. The following code options were used for the calculations presented in this paper: A cell-centered formulation was used for the discretization. Convective fluxes were evaluated by using a second-order-accurate central-differencing scheme with scalar dissipation. Integration in time was performed with an explicit hybrid five-stage multigrid scheme. The turbulence model equations were computed separately from the RANS equations on a single-grid basis. A first-order-accurate Roe flux-difference upwind scheme was used for the convective fluxes of the turbulence equations, and a fully implicit integration scheme was employed for the temporal discretization. Convergence was accelerated by the use of implicit residual smoothing, local time stepping, and multigrid. Both convergence and accuracy were enhanced by low-Mach-number preconditioning. Time-accurate calculations were realized by using a second-order-accurate implicit dual-time-stepping scheme. The Menter baseline (BSL) turbulence model was used for all calculations.

C. Linear Stability Equations Solver LILO

The numerical method used for determining local amplification of disturbances is more general than the stability theory based on the Orr–Sommerfeld equation. LILO [23] treats laminar compressible boundary layers. The boundary layer is assumed to be a parallel flow. The harmonic-wave assumption is applied to the variables u, v, w, p, T,

$$q = \tilde{q}(x, y, z, t) + q'(x, y, z, t), \qquad q'(x, y, z, t) = \hat{q} e^{i(\alpha x + \beta y - \omega t)}$$

where the quantity q is decomposed into the basic state of the boundary layer $\tilde{q}$, which is slowly changing with time, and the single wave mode q'. Assuming that the frequency of the single wave mode is much larger than the frequencies in the temporal distribution of the basic flow state, the time dependence of the evolution matrices of the system of five stability equations can be neglected and the stability problem solved at a discrete time is approximately the same as for stationary basic flow states. LILO solves the linear eigenvalue problem for the complex eigenvalue ω, in which the real wave numbers α and β (for 3D cases) are prescribed by the user. Hence, the temporal stability problem is solved. The system of differential equations is discretized with symmetrical second-order differences. This yields a $5n$-dimensional complex band matrix in which n is the number of grid points in the wall-normal direction. The numerical eigenvalue computation is accomplished with a generalized inverse Rayleigh iteration [24] that takes into account the banded structure of the algebraic problem. The code provides efficient searching strategies that can be used to find the range of unstable modes for a given flow problem. A database method to find the range of amplified spanwise wave numbers is also offered.

D. Transition Prediction for Unsteady Flow

A quite successful method for transition predictions was derived from observations that the location of the final transition phase (breakdown) is, in many cases, dominated by the behavior of the primary instabilities with exponential growth. It was found that the point at which the boundary layer becomes fully turbulent correlates well with a certain amplification factor of the most unstable primary wave that is calculated from the point of neutral stability up to the location with fully turbulent flow. These findings constitute the so-called e^N method [21].

A suitable mathematical formulation of the e^N method may be obtained from kinematic wave theory [25]. Here, only the 2D incompressible flows are considered, in which 2D waves traveling in the x direction exhibit maximum amplification, according to Squire's theorem. By assuming the existence of a differentiable phase function $\theta = \alpha x - \omega t$ of the wave mode and the existence of a dispersion relation $\omega = \Omega(\alpha, x, y, t)$, the real part of the group velocity (which represents the energy propagation of the wave) is obtained as the gradient

$$v_g = \frac{\partial \omega_r}{\partial \alpha_r}$$

The group velocity can be used to define material derivatives of quantities that propagate along with the wave [25]. For stationary basic flow states that vary with x, the frequency of the wave is constant but the wave number varies. For transition analysis of stationary 2D boundary layers over airfoils, it is then straightforward to consider the overall amplification factor $A(x)/A_0$ of the perturbation amplitude A with reference to the amplitude at the neutral point A_0 for a fixed frequency. The so-called N factor is then obtained by taking the maximum value of the amplitude exponent for all unstable modes:

$$N(x) = \max_{\omega} \left(\int_{x_0}^{x} -\alpha_i(x, \omega)\, \mathrm{d}x \right)$$

which forms an envelope over the investigated modes. The point at which the local N factor exceeds the critical value determines the location of breakdown to turbulence. The solution of the temporal stability problem is often preferable to the spatial problem. One can transform temporal growth into spatial growth by using the Gaster transformation [26]:

$$\alpha_i = -\omega_i / v_g$$

Using this relation and computing the change of the exponent Δn of the amplitude ratio over a certain distance Δx, one obtains

$$\Delta n = \int_x^{x+\Delta x} \frac{\omega_i}{v_g}\,\mathrm{d}x$$

With $\mathrm{d}x = v_g\,\mathrm{d}t$, this becomes a time-stepping scheme for the change of n with time:

$$\Delta n = \ell_n \frac{A(x + v_g \Delta t)}{A(x)} = \int_t^{t+\Delta t} \omega_i(x)\,\mathrm{d}t$$

$$n(x + v_g \Delta t) = n(x) + \Delta n$$

Then the new values of n at the position $x + v_g \Delta t$ may be interpolated to any position x (for example, to positions of grid points).

E. Code Implementation and Execution Procedures

1. *Extraction of Boundary-Layer Parameters*

The computation of stability with the LILO code requires the local integral boundary-layer parameters and the local basic flow state. The boundary-layer edge is taken at the point at which the vorticity has reached 0.5% of the maximum value in the flow field, with the search starting from the outside of the boundary layer. This boundary-layer-edge criterion has proven to be very reliable for the thick boundary layers encountered at low Reynolds numbers and is also used in the structured RANS method elsA [27].

The wall-tangential velocity component is then used to calculate boundary-layer parameters such as displacement thickness and momentum thickness. These boundary-layer parameters are transferred to LILO, together with the velocity and temperature profiles (including their derivatives) from the URANS solution at each time step. LILO performs a spline interpolation of the profiles and extracts a specified number of points from the splines. For all computations performed, a number of 50 points for the numerical solution of the stability equations was used.

2. *N Factor for Unsteady Flow*

The unsteady-flow simulation can be started using the results from a preceding steady-N-factor investigation as the starting solution, but it is generally started from scratch, assuming laminar flow. Then, after a boundary layer has formed, the range of amplified frequencies is determined and amplified modes are searched at several positions in the laminar flow. The amplitude exponent is thereafter computed with the preceding time-dependent scheme. Numerically, this is achieved by specifying not only the frequency to investigate, but also using the mode's wavelength and amplification rate from the last time step as the initial value for the current time step. As the frequency range of amplified modes changes during the unsteady-flow computation, the frequency range of new modes is adapted during the computation. To achieve a good frequency resolution at all flow states, an exponential frequency grid with $f_n = f_1 \times 1.15^n$ is used. For the current investigation, the overall range was limited to $f_1 = 50$ Hz and $f_{\max} = 2000$ Hz. Multiple TS modes with different wave numbers and amplification rates may be found by the numerical method for a fixed frequency. All these modes are allowed, because which mode will become dominant during the unsteady computation is not known a priori. The search for new modes is performed 100 times per motion period. This is necessary for cases with large angle-of-attack changes, because modes that might trigger transition at high angles of attack can be damped so strongly at low angles of attack that they diminish to $n = 0$. Accordingly, modes are deleted when they are completely damped to $n = 0$. The occurrence and location of the critical N factor are checked for every single mode n. The most upstream location found is then used as the transition location.

3. *N-Factor Extrapolation*

The numerical update of the transition location requires special attention: Switching on the source terms of the turbulence model at the predicted transition location will numerically affect the laminar boundary layer just upstream of that point. At some flow states, the reduction of amplification rates due to this upstream influence can be large enough to prevent the calculated N factor from reaching the critical value, and hence no transition point is found. As the transition location is then set to the trailing edge, one obtains a stronger amplified laminar region again and thus the transition location moves to the previous position. Linear N-factor extrapolation is used to stabilize the transition location and thus avoid these unphysical oscillations (see Fig. 1). Note that the e^N method itself is an extrapolation technique of linear stability results to the transition point, upstream of which nonlinear effects dominate, in reality. Therefore, a local extrapolation of N factors is an acceptable modification of the overall e^N method. N-factor extrapolation is applied whenever the N factor reaches a limit of $N_{\text{limit}} = 0.9 N_{\text{crit}}$, and in general, the lowest slope found in the range of $0.6 \cdot N_{\text{crit}} < N < 0.85 \cdot N_{\text{crit}}$ is used for the extrapolation, starting at $0.85 \cdot N_{\text{crit}}$. However, at most flow states, there is no need for extrapolation and the original and the extrapolated N factor are virtually the same.

F. Inviscid Unsteady Airfoil Theory

The development of analytical inviscid unsteady airfoil theory was motivated by the problem of flutter instabilities that became important shortly after the beginning of aviation. The first analytical theory for the calculation of unsteady aerodynamic forces for a harmonic oscillating airfoil was given in 1922 by Birnbaum [28] and later expanded for the calculation of higher-frequency motions by Küssner [14,29]. A corresponding theory was given independently by Theodorson [30].

The basic idea of the theory is to prescribe a time-dependent bound circulation, and the change in bound circulation has to correspond to the convection of free circulation, due to Helmholtz's circulation theorem. Then the additional velocities induced on the airfoil (due to the free circulation in the wake), and thus the unsteady forces, can be calculated. The same assumptions as in Prandtl's lifting-line theory apply; thus, it is a theory of small disturbances and is valid for small angles of attack only. Some fundamental results of the theory are as follows:

1) The thrust gained and the efficiency are independent of the mean angle of attack.

2) A pure pitching motion cannot generate thrust.

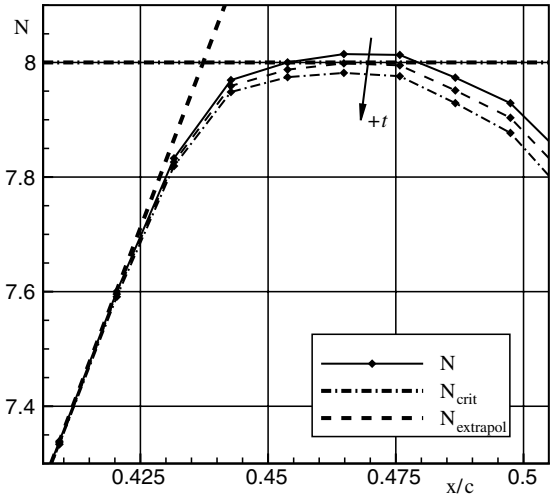

Fig. 1 *N*-factor extrapolation.

3) For small frequencies, a phase shift between pitch and plunge motion of 90 deg is optimal, corresponding to the early observations of Lilienthal [31].

4) The propulsive efficiency of the pure plunging motion approaches unity when the frequency approaches zero, and it approaches 50% when the frequency approaches infinity.

5) The propulsive efficiency is constant for a constant ratio of pitch and plunge amplitude.

6) The best propulsive efficiency of a combined plunge and pitch motion is unity for all frequencies, but with the thrust approaching zero.

The present work uses results of Küssner's [14] theory as a guideline for evaluation of favorable motion parameters.

III. Motion Parameters and Definition of Coefficients

With the z axis perpendicular and the x axis parallel to the freestream velocity, the plunge motion of the airfoil is prescribed as

$$z(t) = z_1 \cos\left(2\pi \frac{t}{T}\right)$$

The pitch motion is defined as

$$\alpha(t) = \alpha_0 + \alpha_1 \cos\left(2\pi \frac{t}{T} + \varphi\right)$$

The resulting plunge/pitch motion for a phase shift of $\varphi = 90$ deg and a mean angle of attack of $\alpha = 0$ deg is depicted in Fig. 2.

No motion in the x direction is prescribed; thus, $x(t) = \text{const}$. Another parameter to describe the motion of a wing is the reduced frequency:

$$k = \frac{\pi f c}{U_\infty}$$

For small reduced frequencies, flows are quasi-steady. This means that the flow around the airfoil is always supposed to behave like the stationary flow at the current angle of attack. Then for every point in time, an effective velocity and an effective angle of attack can be calculated. The resulting angle of attack ζ caused by the translatory movement can be calculated as

$$\zeta(t) = \arctan\left(\frac{-\dot{z}(t)}{U_\infty}\right) = \arctan\left(2k\frac{z_1}{c}\sin\left(2\pi\frac{t}{T}\right)\right)$$
$$\approx 2k\frac{z_1}{c}\sin\left(2\pi\frac{t}{T}\right) = \zeta_1 \sin\left(2\pi\frac{t}{T}\right)$$

using the small-angle approximation. For larger angles, $\zeta_{1L} = \zeta_{\max} = \arctan(2k(z_1/c))$ can be used.

The effects of the translative and pitch motions can be added to obtain an effective angle of attack. Using a phase shift of $\varphi = 90$ deg, it follows that

$$\alpha_{\text{eff}} = \alpha(t) + \zeta(t) \approx \alpha_0 + (\zeta_1 - \alpha_1)\sin\left(2\pi\frac{t}{T}\right)$$
$$= \alpha_0 + \Delta\alpha_{\text{eff}}\sin\left(2\pi\frac{t}{T}\right)$$

introducing the effective amplitude $\Delta\alpha_{\text{eff}}$. A useful combined parameter is the amplitude ratio

$$\lambda = \frac{\alpha_1}{2k\frac{z_1}{c}} = \frac{\alpha_1}{\zeta_1} \approx \frac{\alpha_1}{\zeta_{1L}} = \lambda_L$$

The effective velocity is

$$U_{\text{eff}} = \sqrt{U_\infty^2 + \dot{z}^2} = U_\infty\sqrt{1 + \zeta_1^2\sin^2\left(2\pi\frac{t}{T}\right)}$$

$$U_{\text{eff,max}} = U_\infty\sqrt{1 + \zeta_1^2}$$

The force coefficients in the x and z directions, moment coefficient, and power coefficient can be defined as

$$c_x = \frac{F_x}{\rho/2cU_\infty^2}, \qquad c_z = \frac{F_z}{\rho/2cU_\infty^2}, \qquad c_m = \frac{M_y}{\rho/2c^2U_\infty^2}$$

$$c_\pi = \frac{P}{\rho/2cU_\infty^3}$$

These can be used to define a thrust coefficient, taking the steady drag of the airfoil into account:

$$c_T^* = -c_x + c_{x,\text{stat}}(\alpha_0)$$

The propulsive efficiency is defined as

$$\eta_P = \frac{\bar{c}_{\pi,\text{out}}}{\bar{c}_{\pi,\text{in}}} = \frac{(1/TU_\infty)\int_0^T c_T^* U_\infty \,\mathrm{d}t}{(1/TU_\infty)\int_0^T (c_z\dot{z} + c_m\dot{\alpha}c)\,\mathrm{d}t} = \frac{\bar{c}_T^*}{\bar{c}_{\pi,\text{in}}}$$

The idea behind this definition is to compare a flapping-wing vehicle with a conventional propeller-driven vehicle, for which thrust and drag are independent of each other. Thus, the steady-state correction refers to the lowest possible drag a propeller-driven vehicle would have using an appropriate airfoil.

It should be pointed out that other definitions exist for the propulsive efficiency that only take the frictional part of the steady drag $c_{d,f}$ into account. At low Reynolds numbers, the pressure part of the steady drag $c_{d,p}$ cannot be neglected; therefore, the complete steady drag $c_{x,\text{stat}} = c_d(\alpha_0)$ is used for the correction. Without a correction using the steady drag, the efficiency would become zero for a steady-state flight ($c_x = 0$), which is an obviously meaningless result.

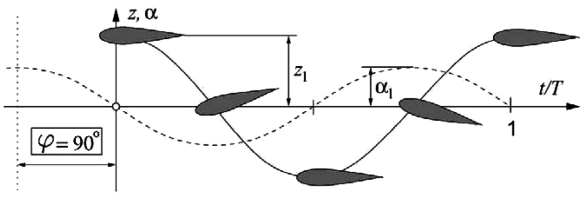

Fig. 2 Sketch of a combined plunge/pitch motion with $\varphi = 90$ deg and $\alpha_0 = 0$ deg.

IV. Results and Analysis

A. Verification and Validation of the Numerical Simulations

Results of the verification [19,32] and validation [19,32,33] for the steady-incoming-flow case have already been published; two validation cases for the moving airfoil with a pure plunge motion were presented in [19]. Only a very brief overview of these results will be given here. The focus in this section will be on the verification for the moving airfoil case. A third validation case with pure plunge motion will also be presented here, denoted as case III.

The computational mesh for the numerical investigation of the SD7003 airfoil flow contains 1008×216 cells on the finest-grid level, whereas most computations were performed on the second grid level, with 504×108 cells. The grid is adapted to the expected flow features to have a good resolution of the LSBs over a range of incidence angles. Compared with the previous studies, the number of points was slightly reduced, to save some computational time in the parameter study for the moving airfoil. Also, the first spacing at the leading edge was reduced to get a good resolution of the boundary layer at very large angles of attack, for which flow separation can occur right at the leading edge. Figure 3 shows the mesh on the fourth grid level in the vicinity of the airfoil. The far-field distance is 20 times the chord length.

The freestream Mach number was set to a value of 0.05, with low-speed preconditioning to simulate incompressible flow. Previous computations indicated that this Mach number is low enough to exclude compressibility effects and there is no need to adapt the value

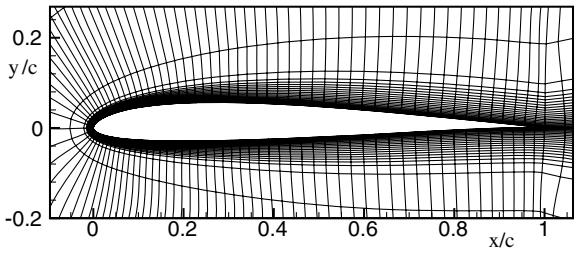

Fig. 3 Computational mesh with 160 × 21 cells.

to specific wind-tunnel or water-tunnel situations. For large LSBs encountered at $Re = 60,000$ and for stationary onflow, no converged results were obtained on the fine-grid levels using the RANS solver in its steady mode. Therefore, all computations were performed in the time-accurate mode based on the dual-time-stepping approach.

In the case of stationary onflow, there is generally no need to predict transition at every time step, and thus the CPU percentage for the transition prediction (∼5%) is negligible. Transition prediction for the fully time-accurate solutions in the case of the moving airfoil caused a CPU percentage of around 45%.

1. Validation Results for Steady Incoming Flow

The focus of interest in validation is on the growth rate of turbulence within the transition region from laminar to fully turbulent shear layers and on the levels of shear stress around reattachment at the end of the bubble. The turbulent shear stress $\tau_{xy} = -\rho\overline{u'v'}$ causes transport of momentum across the boundary layer, which is responsible for the closure of the LSB.

The transition location in the measurements is defined as the beginning of the turbulent wedge that spreads from the shear layer of the LSB. In particular, the point is taken at which the normalized Reynolds shear stress obtains 0.1% and demonstrates a clearly visible rise. Otherwise, measurement errors due to insufficient resolution of the flapping of the laminar part of the LSB could be misinterpreted as turbulent flow.

The measured and computed LSBs and the corresponding shear stress distributions for an angle of attack of 4 deg are displayed in Fig. 4. The experimental data were taken in the low-disturbance wind tunnel (LNB) at the Technical University of Braunschweig;[§] therefore, a rather large value of the critical N factor $N_{\text{crit}} = 10$ seems appropriate. Note that very similar experimental results were obtained by Ol et al. [34] in two water facilities. For several angles of attack investigated, the best overall performance was found [32,33] for the Menter BSL turbulence model.

Temporal fluctuations of the LSB were resolved using a small time step. Inspection of the temporal development of the numerical solution indicates that a Kelvin–Helmholtz instability was resolved in the laminar part of the LSB, which appears as vortex shedding in Fig. 4. The frequency of the vortex shedding, the most amplified frequency calculated with LILO, and the dominant frequency of 2D waves captured using time-resolved particle image velocimetry (PIV) [35] were found to agree reasonably well. A similar result was already found by Watmuff [36], in which the shedding frequency compared well to the frequency of the most amplified mode predicted by inviscid linear stability theory. Vortex shedding due to a KH instability has also been observed in numerical simulations of the low-Reynolds-number flow on a Eppler E387 airfoil by other authors [37,38].

Using a large time step, the KH instability is not resolved, and thus a steady state is reached. The solution shows only a minor difference to a time-averaged solution using the small time step. The direct resolution of the KH instability provides an additional mechanism of momentum transport to the wall and thus helps to close the LSB. However, the initial disturbance for the KH instability is most likely

[§]Data available online at http://www.tu-braunschweig.de/ism/institut/wkanlagen/lnb/index.html [retrieved 2008].

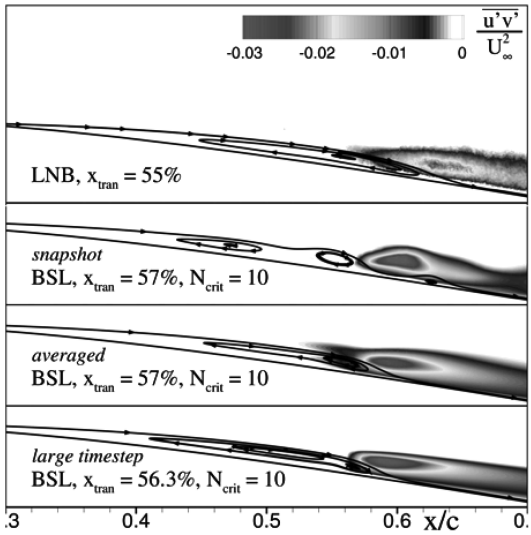

Fig. 4 Experimental and numerical streamlines and turbulent shear stress for $\alpha = 4$ deg.

"numerical noise" and cannot be controlled by the user. Hence, in simulations of freestream flow with very low turbulence, the LSB is closed by direct resolution of the KH instability upstream of the point at which the N factor calculated by LST becomes N_{crit}. Thus, there is an upper limit for N_{crit} with our present URANS-equation approach.

2. Lift and Drag Coefficients

The computed force coefficients are compared with the measured data by Selig et al. [39–42] in Fig. 5. It is noticeable that the measurements in the tunnels at the University of Illinois at Urbana–Champaign and Princeton University gave rather different results, even though both test sections and models had approximately the same size and turbulence level, appropriate wall corrections were applied, and end plates were used. For the low Reynolds number of $Re = 60,000$, it was found in the Illinois measurement that the wake flow was not two-dimensional, resulting in a strong influence of the spanwise measurement position on the drag coefficient [43].

Given the uncertainty in the measured coefficients, the calculated values agree well. For the low angles of attack, although LSBs with different sizes were calculated depending on the turbulence model applied (not shown here), the computed drag coefficients differ only slightly. Obviously, the contribution of an elevated pressure drag for a larger bubble is compensated by a reduced friction drag, due to the larger and stronger recirculation area. For the higher angles of attack, the pressure drag becomes dominant and the bubble size is more

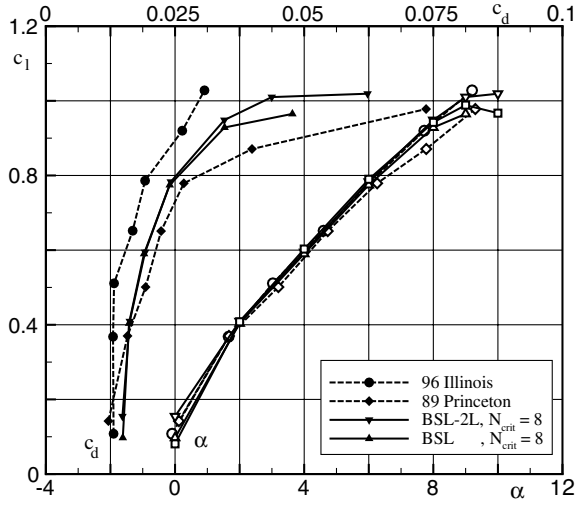

Fig. 5 Computed and measured force coefficients.

important. The best agreement with PIV measurements was found using the Menter BSL model. To improve the performance of the BSL model at higher angles of attack, it was used in a so-called two-layer mode (BSL-2L), as proposed by Menter [44]. With this variant, the blending from the ω length-scale equation that is used close to the wall to the ε equation in the outer boundary-layer region is located closer to the wall. This yields a later onset of turbulent flow separation and thus a slightly larger lift coefficient near α_{max}.

3. *Validation Results for the Moving Airfoil*

The validation cases I and II presented in [19] were designed to yield a moderate and a strong movement of the transition location, with the effective angle of attack well inside the airfoil's operational range for steady onflow. The case presented here (denoted as case III) was designed to be more extreme, pushing toward the limitations of the method. This experiment was also performed in the water tunnel (WUB) at the Technical University of Braunschweig.¶ The mean angle of attack for this case is $\alpha_0 = 8$ deg, the plunging amplitude is $z_1/c = 0.1$, and the reduced frequency is $k = 0.797$. The resulting quasi-steady equivalent effective angle of attack for the airfoil motion then reads $\alpha_{eff} \approx 8\,\text{deg} + 9.1\,\text{deg}\sin(2\pi(t/T))$. Phase-locked PIV measurements were performed at $t/T = 0$, 0.25 (downstroke, $\alpha_{eff} \approx 17.1$ deg), 0.375, 0.5, 0.75, and 0.875. For $t/T = 0$, no transition was found inside the measurement window starting at $x/c = 0.61$. To draw streamlines, the v component of the velocity is corrected with the plunging velocity of the airfoil, leading to a velocity of zero on the surface of the airfoil.

To take into account the wall effect from the water-tunnel experiment, a simple wall correction for steady flows [45] was applied. This results into an effective angle of attack of $\alpha_{eff} \approx 8.6\,\text{deg} + 9.8\,\text{deg}\sin(2\pi\frac{t}{T})$, corresponding to a plunging amplitude of $z_1/c = 0.107$, which was used for the calculations. For case I, a critical N factor of $N_{crit} = 6$ gave a very good agreement in transition location between measurement and calculation, whereas it was rather too high for case II [19]. Thus case III was calculated for $N_{crit} = 4$ and 6.

Figure 6 displays the temporal distributions of transition location, the frequency of the TS mode that triggers transition and force coefficients. The experimental transition locations for these phase-locked measurements were determined as with the measurement at steady onflow conditions, as described earlier. Although the calculated and measured transition locations agree quite well for both values of N_{crit}, there is a huge difference in the horizontal-force component, due to a much larger LSB and significantly thicker boundary layer in the case of $N_{crit} = 6$. A comparison with the measured LSB in the middle of downstroke ($t/T = 0.25$) gives a good agreement with the calculation with $N_{crit} = 4$ (see Fig. 7). The dominant TS modes encountered for this case have an extreme frequency range from 100 to 1800 Hz. Unsteady transition prediction would not have been possible for this case without the search for new TS modes during the computation.

4. *Verification Results for the Airfoil with Pitch and Plunge Motion*

Two cases with moderate amplitudes were chosen for verification. The parameters of the first case are $k = 0.25$, $\alpha_0 = 4$ deg, $\zeta_{1L} = 20$ deg, $\alpha_1 = 14$ deg, $\varphi = 90$ deg, $\lambda_L = 0.7$, $\Delta\alpha_{eff} = 6$ deg, and $N_{crit} = 8$. At this rather low frequency, a fully periodic solution is found in the third motion period (not shown). At first, a grid convergence study was performed, running the case on the first (1008×216), second (504×108), and third (252×54) grid levels. The difference between the results from the first and second grid levels, as seen in Fig. 8, are small enough to justify the use of the second grid level to obtain engineering results in a parameter study. The dependence of the results from the number of time steps per motion period is investigated next. For all cases, a search for new modes was performed 125 times per period. To avoid numerical errors, the energy propagation of each TS mode $v_g \Delta t$ is restricted to

¶Data available online at http://www.tu-braunschweig.de/ism/institut/wkanlagen/wub/index.html [retrieved 2008].

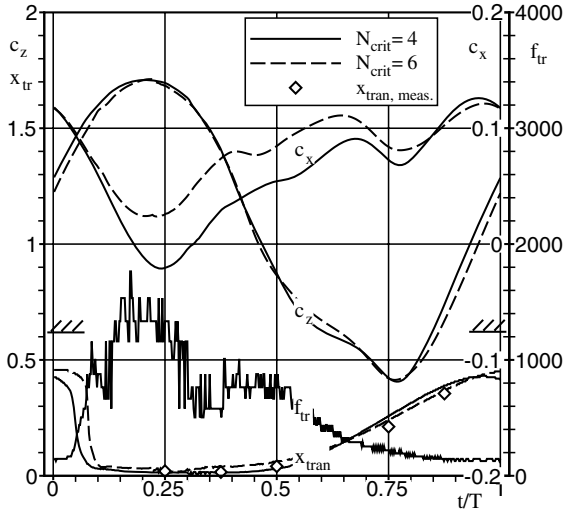

Fig. 6 Transition locations, transition frequencies, and computed force coefficients for unsteady case III.

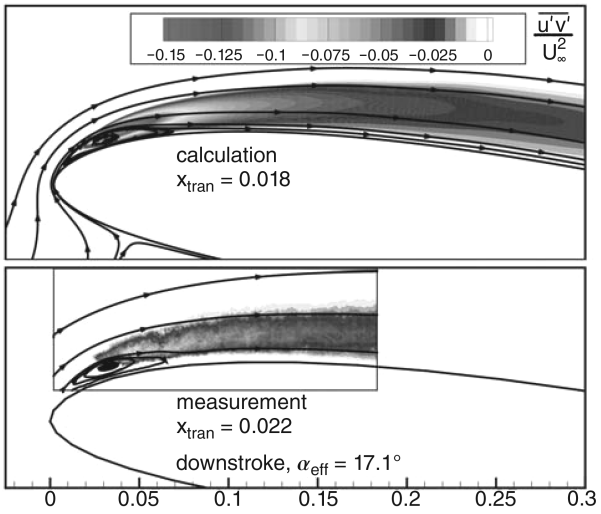

Fig. 7 Comparison of streamlines and turbulent shear stress at downstroke for case III.

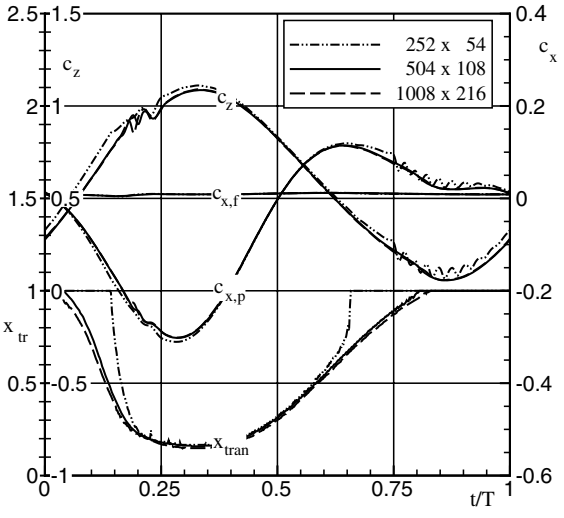

Fig. 8 Grid convergence study for verification case I.

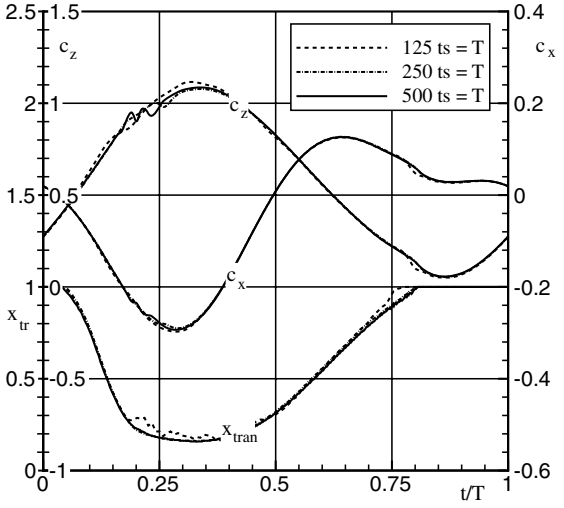

Fig. 9 Time accuracy of verification case I.

1% of the chord length. This means that subtime steps are calculated in the temporal scheme for the amplitude exponent n if the temporal resolution for the main flow is too low. At $k = 0.25$ and for high group velocities encountered at the suction peak close to the leading edge, about 2–3 subtime steps are required when the main flow is resolved by 500 time steps. The results shown in Fig. 9 indicate that time accuracy is reached using 250 time steps per period, except for a local phenomenon at $t/T \approx 0.2$. At this time, transition reaches a LSB that has formed close to the leading edge during the downstroke of the airfoil. Although the LSB is shortened by the onset of turbulence, it sheds a single vortex, which is then convected downstream.

Finally, a run using the transition-prediction approach for steady incoming flow was also performed. The result is compared with the unsteady transition approach in Fig. 10. Although transition starts moving upstream somewhat later for unsteady transition, there is nearly no difference in transition location once it gets closer to the suction peak at the leading edge. This is explained by the high group velocities, as well as by the shorter distance between indifference and the transition point. Both have the effect of taking only a short time for disturbance energy to propagate through the amplified region of the laminar boundary layer, and therefore there is no relevant unsteady effect on transition. An unsteady effect is seen for the transition frequency, which is slightly lower for the unsteady transition prediction. Because the airfoil investigated shows little sensitivity to the size of a bubble encountered around midchord, the difference in transition location at the beginning of the motion period has only a slight effect on the calculated force coefficients. It remains to be seen if other airfoils respond more sensitively to such small differences in the transition location or if an unsteady scheme for transition prediction is generally unimportant at low reduced frequencies.

The parameters of the second verification case are $k = 1.0$, $\alpha_0 = 4\,\text{deg}$, $\zeta_1 = 15\,\text{deg}$, $\alpha_1 = 6\,\text{deg}$, $\varphi = 90\,\text{deg}$, $\lambda = 0.4$, and $N_{\text{crit}} = 4$. The investigation of time accuracy and a grid convergence study gave the same result as for the first verification case. Because this results in a four-times-shorter time step, KH instabilities are resolved and LSBs tend to shed vortices, which results in higher-frequency oscillations in the force coefficient. To get clear verification results, vortex -shedding was suppressed by the use of an N factor of only $N_{\text{crit}} = 4$ and thus a reduced size of the LSBs. The comparison between steady and unsteady transition prediction for this case is shown in Fig. 11. A much stronger difference in transition location is found now, with transition starting to move upstream about a quarter of a period length earlier in the case of steady transition prediction. Only a slight difference remains when transition gets closer to the leading edge, for the same reasons as before. Surprisingly, there is still very little difference between the calculated force coefficients. The upstream jump of transition location in two discrete steps for the unsteady transition seems

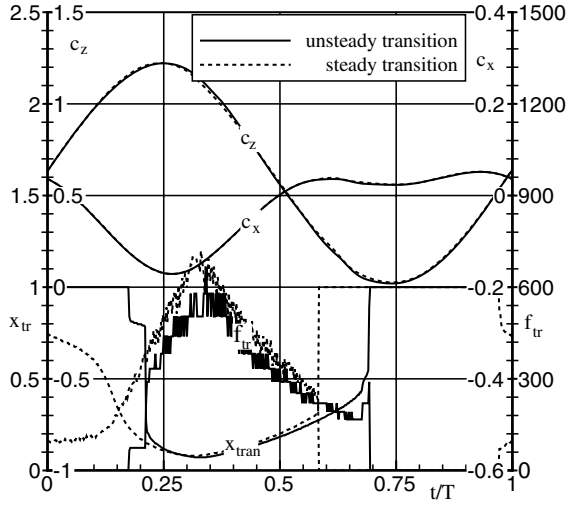

Fig. 11 Steady and unsteady transition prediction for verification case II, $k = 1.0$.

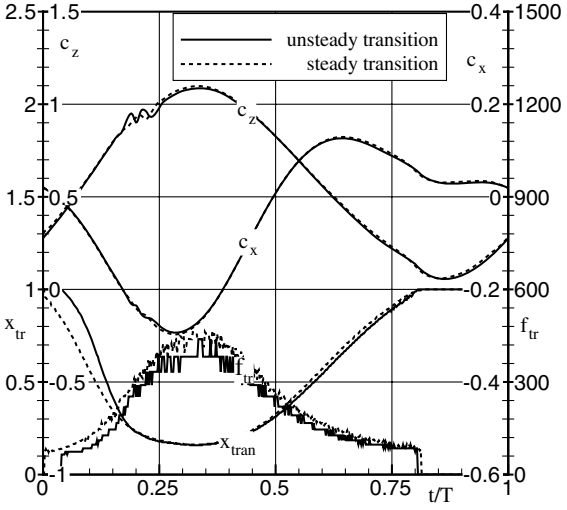

Fig. 10 Steady and unsteady transition prediction for verification case I, $k = 0.25$.

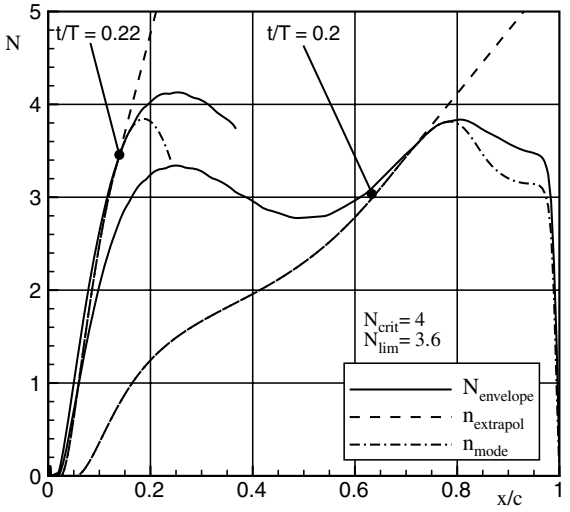

Fig. 12 Amplitude exponents N and n during downstroke.

strange at first sight, but is in fact a flow feature at a higher reduced frequency.

This is illustrated in Fig. 12, in which the amplitude exponents for the envelope over all TS modes N, as well as the single modes n that cause transition, are shown for $t/T = 0.2$ and 0.22. At $t/T = 0.2$, the remains of a LSB that has formed during the downstroke of the last motion period and then convected downstream is reamplified and causes transition at $x/c = 0.8$, due to a TS mode with a frequency of 74 Hz. Shortly after, a new laminar separation that was growing during the downstroke causes another TS mode at 290 Hz to trigger transition at $x/c = 0.2$ and thus forms a new LSB close to the leading edge. A variation of the amount of numerical dissipation within the usual range showed no effect on the solution at all.

B. Parameter Study

The main goal of the parameter study is to quantify the additional losses due to airfoil drag compared with inviscid unsteady airfoil theory. Viscous flow cases with high propulsive efficiencies are searched in a thrust range up to about 10 times the stationary onflow airfoil drag. If a 2D case produces net thrust, it could be misinterpreted as a violation of the presumed steady-state flight at constant velocity. Instead, it should rather be interpreted as a thrust reserve to overcome the additional induced drag in a hypothetical 3D application or to accelerate in a 2D case.

The correction value of $c_{x,\mathrm{stat}} = 0.0192$ for the calculation of propulsive efficiency was taken from the stationary onflow case at $\alpha = 4$ deg, which is the mean angle of attack α_0 for all cases of the parameter study. Although the mean lift obtained for some cases differed from the stationary lift at $\alpha = 4$ deg, there was no need to adapt the correction value for every case according to the drag polar gained at stationary onflow. This will be discussed later. Also, the airfoil SD7003 chosen for this study shows a good performance for stationary flow. Thus it is assumed that the calculated propulsive efficiencies do not benefit from an unsteady drag reduction.

The parameter study was performed for three reduced frequencies of $k = 0.25, 0.5$, and 1.0. For all cases, 500 time steps per period were used for stability reasons. In consequence, it is inevitable that vortex shedding due to KH instabilities is resolved for the high reduced frequency of $k = 1.0$. To enforce closure of LSBs due to the modeled turbulence, the critical N factor was set to $N_{\mathrm{crit}} = 8$. A higher critical N factor would have been possible at $k = 0.25$, because no vortex shedding due to a KH instability occurred. However, the same critical N factor was used for the lower frequencies for comparability. $N_{\mathrm{crit}} = 8$ corresponds to a turbulence level of $Tu \approx 0.1\%$, which is encountered in low-turbulence wind tunnels, but might be too small to simulate the flow in free atmosphere. All calculations were performed on the second grid level using 504×108 grid points. To achieve a periodic solution, three motion periods were required at $k = 0.25$, four at $k = 0.5$, and eight at $k = 1.0$. All calculations were performed at a Reynolds number of $Re = 60,000$.

1. *Low Frequency, $k = 0.25$*

Küssner [14] stated that because the drag of an airfoil is a symmetrical function of the angle of attack, the mean airfoil drag of a moving airfoil will always be higher than the drag of an airfoil at the mean angle of attack. Also, he stated that this loss due to airfoil drag can be of the same magnitude as the vortex losses.

To quantify how the additional drag losses increase with the angle-of-attack range used, sets of computations were performed in which the angle-of-attack range was the same and the motion amplitudes were increased. Thus, the maximum angle of attack from plunging ζ_{1L} was reduced by a pitch motion to get fixed effective amplitudes $\Delta\alpha_{\mathrm{eff}} = \zeta_{1L} - \alpha_1$. As can be seen in Fig. 13 by a comparison to results obtained using Küssner's [14] theory, the offset between the curves and thus the additional drag loss increases with increasing effective amplitude. Because of the dynamic stall effect, there is no major separation at the maximum effective angle of attack of $\alpha_{\mathrm{eff,max}} = \alpha_0 + \Delta\alpha_{\mathrm{eff}} = 14$ deg encountered during downstroke, whereas the angle of attack for maximum lift at steady-state conditions is at about $\alpha_{c_a,\mathrm{max}} \approx 11$ deg.

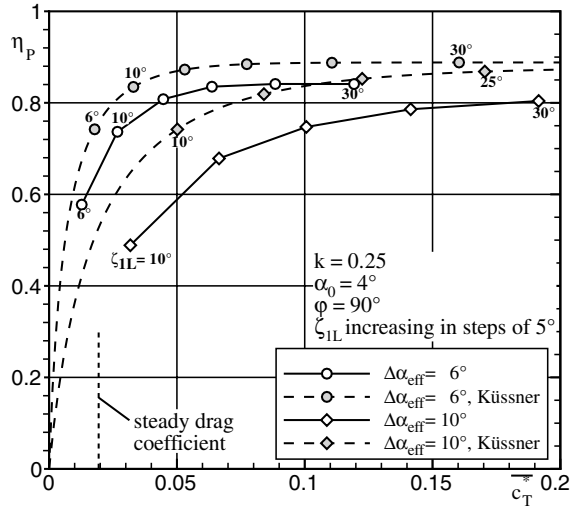

Fig. 13 Thrust and propulsive efficiency for constant effective amplitudes and $k = 0.25$.

According to Küssner's [14] theory, the maximum efficiency for $k = 0.25$ is gained at a phase shift between pitch and plunge motion of $\varphi = 80$ deg. Accordingly, a set of calculations was performed for $\Delta\alpha_{\mathrm{eff}} = 6$ deg and with a phase shift of $\varphi = 80$ deg. As can be seen in Fig. 14, a slight improvement of the propulsive efficiency was gained. The reason for this improvement is that the aerodynamic phase shift between motion and forces is compensated at $\varphi = 80$ deg (see Fig. 15). Also shown in Fig. 14 are the results from a variation of the critical N factor between $N_{\mathrm{crit}} = 4$ and 14. Because different correction factors gained from according stationary onflow calculations were used, only a slight variation in propulsive efficiency and thrust is encountered up to $N_{\mathrm{crit}} = 12$. For $N_{\mathrm{crit}} = 14$, the drag produced by the LSB formed during downstroke seems to be so large that the mean airfoil drag for the moving airfoil is largely increased compared with the steady-state drag at mean angle of attack, leading to a significant drop in propulsive efficiency.

Because Küssner's [14] theory gives a constant efficiency using a constant amplitude ratio λ, independently of the motion amplitudes used, additional computations were performed in this direction. Because the previous cases were set up using the definition for large angles ζ_{1L}, the amplitude for large angles λ_L is varied instead of λ. As can be seen in Fig. 16, the propulsive efficiency is nearly constant for a fixed amplitude ratio within the investigated range of thrust coefficients. Both efficiency and thrust coefficient are lower for the FLOWer calculations than those given by Küssner's theory, because

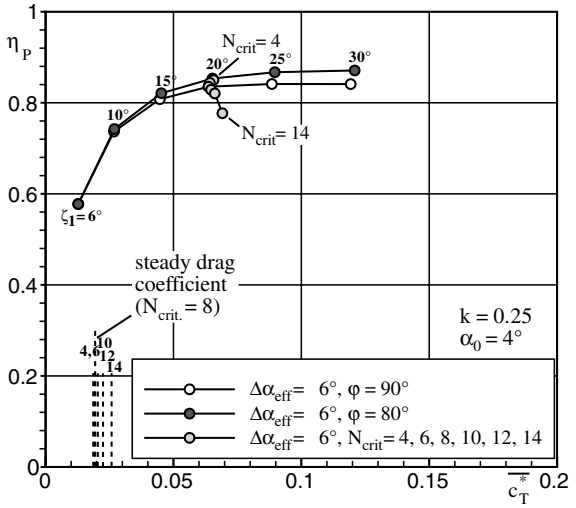

Fig. 14 Influence of motion phase shift φ and N_{crit} on the propulsive efficiency.

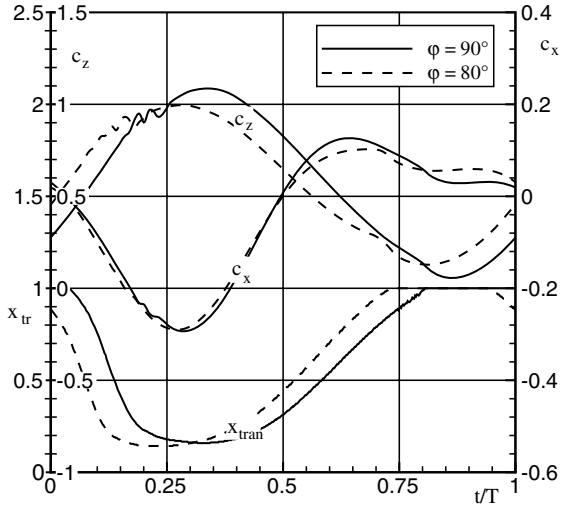

Fig. 15 Influence of the motion phase shift φ on the force coefficients and transition location.

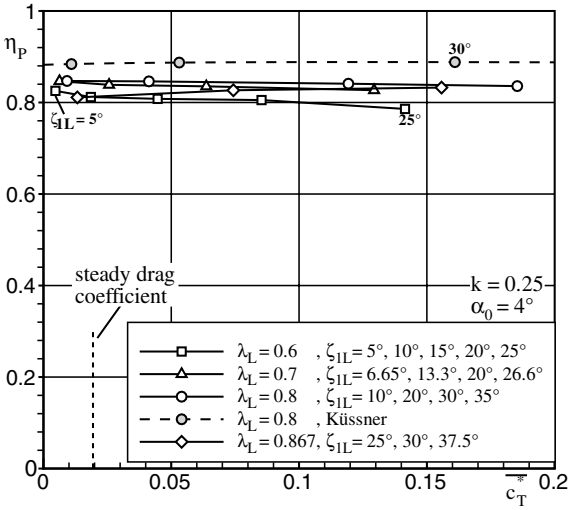

Fig. 16 Thrust and propulsive efficiency for constant amplitude ratios λ_L and $k = 0.25$.

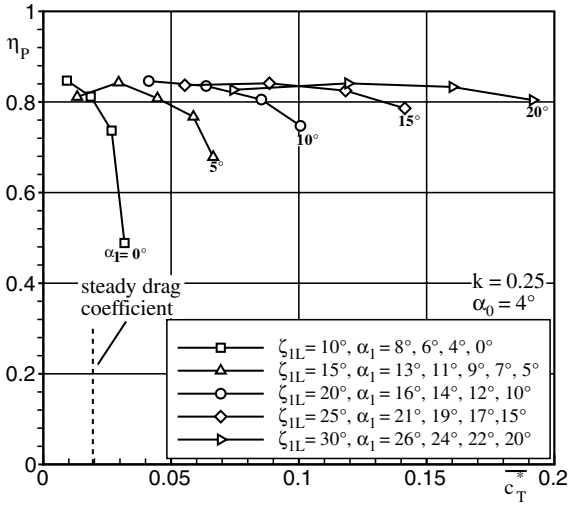

Fig. 17 Thrust and propulsive efficiency for constant plunging amplitudes and $k = 0.25$.

of the airfoil drag. The best efficiency is found for an amplitude ratio of $\lambda_L \approx 0.8$.

For practical applications, it might prove difficult to control the thrust by changing both plunging and pitching amplitude to maintain a good efficiency. Instead, it would be useful to use a fixed plunging amplitude and only control the pitch amplitude, which is illustrated in Fig. 17. Using a large plunging amplitude, the thrust can be regulated over a large range with only small changes in pitch amplitude, whereas the amplitude ratio is kept in the range of high efficiencies.

Although thrust generation and efficiency are of general interest for a propulsion system, lift generation also needs to be addressed in the context of MAVs. In inviscid unsteady airfoil theory, the mean lift depends only on the mean angle of attack α_0. Thus, for the viscous case, a mean lift close to the lift at mean angle of attack and steady incoming flow can be expected: $c_l(\alpha_0 = 4\,\text{deg}) = 0.60$. The obtained mean lift coefficients $\overline{c_z}$ are depicted in Fig. 18 for several effective amplitudes, with the motion amplitudes rising along each curve. Flow separations are getting stronger or rather have a more adverse effect with an increasing effective amplitude, thus a loss of lift is encountered and the curves for a higher effective amplitude obtain a lower lift level. Along the curves for a constant effective amplitude, the lift is slightly rising with increasing motion amplitudes. This effect shows the limitation of the approach using effective amplitudes, which required the assumption of quasi-steady flow behavior. This assumption is only approximately fulfilled at $k = 0.25$. There seem to be several reasons for the rise of lift along these curves: one is a slightly earlier transition with increasing amplitudes and thus a smaller LSB between downstroke and upper dead center, resulting in a stronger suction peak and thus contributing to the mean lift coefficient. Another reason is an increasing aerodynamic phase shift between forces and motion. This results in a higher lift force amplitude and, surprisingly, in a higher lift in the period mean.

The rather strong variations in lift encountered in Fig. 18 put into question the way the propulsive efficiency is calculated (see Sec. III), because for all cases, the same thrust correction $c_{x,\text{stat}}(\alpha_0)$ was used, assuming this to be the drag at steady-state flight with $c_l(\alpha_0) = 0.60$. A better way might be to use $c_{x,\text{stat}}(\overline{c_z})$. However, this would not have had a strong effect on the calculated efficiencies, because the drag coefficient only varies slightly in the region of the obtained mean lift coefficients. Also, it would make no difference for the more efficient parameter combinations. As can be seen in Fig. 19, the efficient cases with $0.6 < \lambda < 0.867$ all give a mean lift coefficient of $\overline{c_z} \approx 0.6$ for the lower thrust coefficients. For an increasing thrust coefficient, the calculated efficiency becomes nearly independent of a small variation in the correction value. Thus, the usage of a constant correction value can be justified.

From the point of practical application, there is a slight drawback to using the motion forms that were investigated. This is shown in

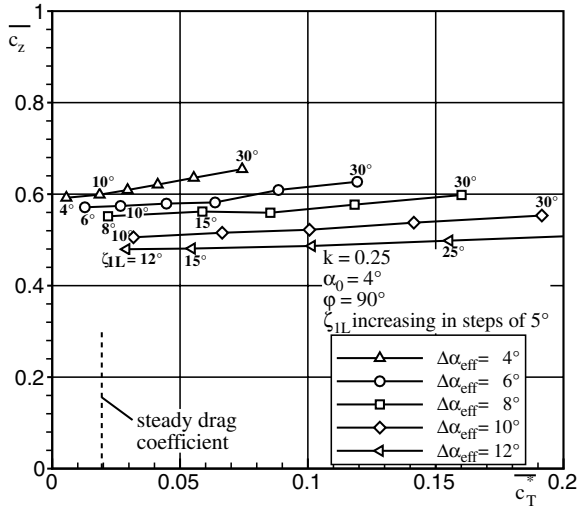

Fig. 18 Thrust and lift for constant effective amplitudes and $k = 0.25$.

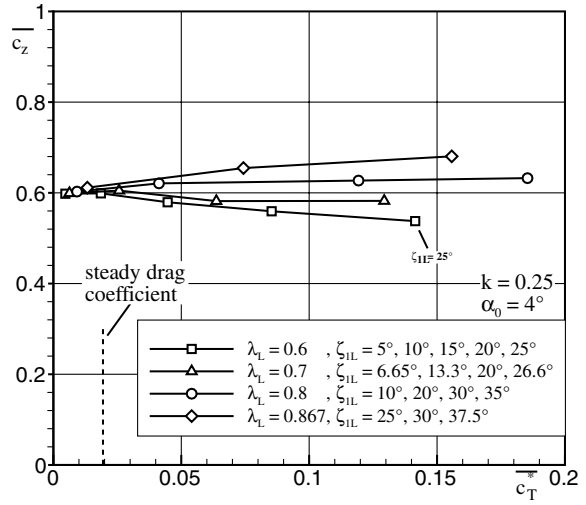

Fig. 19 Thrust and lift for constant amplitude ratios λ_L and $k = 0.25$.

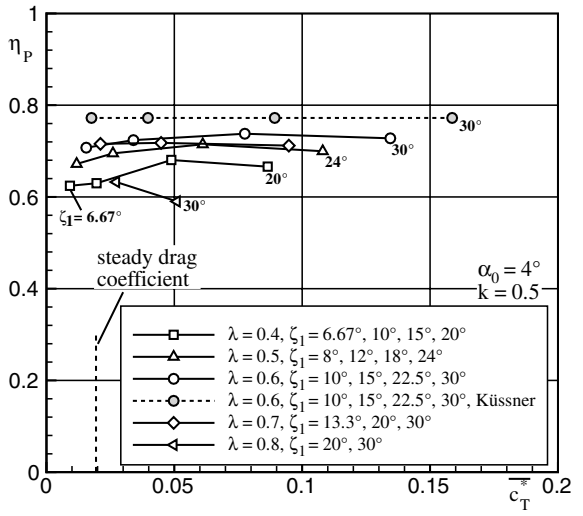

Fig. 21 Thrust and propulsive efficiency for constant amplitude ratios λ and $k = 0.5$.

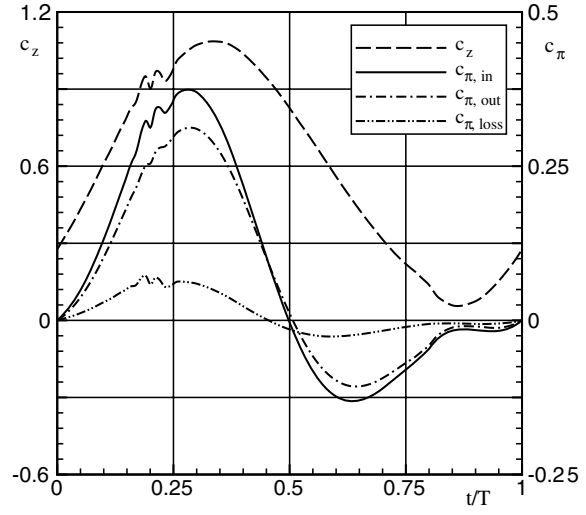

Fig. 20 Instantaneous power coefficients, motion parameters of the first validation case.

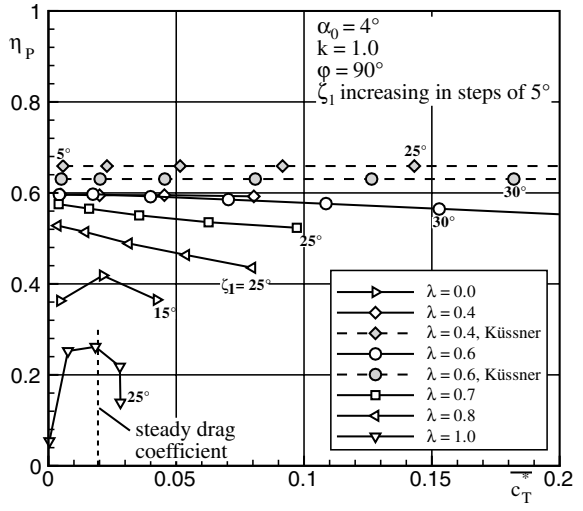

Fig. 22 Thrust and propulsive efficiency for constant amplitude ratios λ and $k = 1.0$.

Fig. 20, in which the instantaneous power coefficients are plotted over the period length. As can be seen, the input power and the power loss are negative during the upstroke. This would require the propulsion system to work as a generator to reach the calculated efficiency, because power is drained from the flow. However, this could be circumvented by using a nonharmonic motion form with a faster upstroke or by using an unforced upstroke driven by the horizontal force. It is known from birds that the upstroke is not only faster than the downstroke, but they also have weaker muscles for upstroke than for downstroke.

2. Medium Frequency, $k = 0.5$

Only a few computations were performed at $k = 0.5$, with the results given in Fig. 21. As for the lower frequency, nearly constant propulsive efficiency is calculated in the investigated thrust range for a constant amplitude ratio λ. Efficiency has dropped due to the larger vortex losses at this higher frequency, and the best efficiency is found at $\lambda \approx 0.6$. The offset to the Küssner [14] results and thus the drag losses are of the same size as for the lower frequency.

3. High Frequency, $k = 1.0$

Calculated thrust coefficients and propulsive efficiencies at a reduced frequency of $k = 1.0$ are shown in Fig. 22, again for fixed amplitude ratios λ. There is a trend of degrading efficiency for increasing amplitudes at this frequency, getting stronger with increasing λ. The best efficiency given by the FLOWer calculations is found around $0.4 \leq \lambda \leq 0.6$. In the range of these optimal amplitude ratios, the losses in efficiency and thrust compared with the Küssner [14] results are comparable with those found at the lower frequencies. Some cases with high amplitudes were calculated, reaching a maximum thrust coefficient of over 0.4 (see Fig. 23). For these cases, both amplitude ratio definitions λ and λ_L were used. Using $\lambda_L = \text{const}$, a lower decrease of efficiency with increasing amplitudes was obtained than for $\lambda = \text{const}$. However, with only one value of the amplitude ratio tested, it cannot be determined which definition is better suited to yield amplitude-independent propulsive efficiencies, as given by Küssner's theory. For a fixed pitching amplitude of $\alpha_1 = 24$ deg, the definition of λ_L increases the plunging amplitude from $z_1/c = 0.35$ to $z_1/c = 0.42$. This 20% increase in amplitudes gives a 60% increase in thrust. As already shown for $k = 0.25$, this gives the opportunity to control the amount of thrust by only slightly changing the motion amplitudes while maintaining good propulsive efficiency.

Finally, the motion phase shift φ was varied for the fixed amplitude ratios of $\lambda = 0.4$ and 0.7. The maximum efficiency predicted by Küssner's [14] theory is found at $\varphi \approx 45$ deg and $\lambda \approx 0.7$ (see Fig. 24). Although the maximum predicted efficiency is always 100%, this point is of no practical use because the predicted thrust is

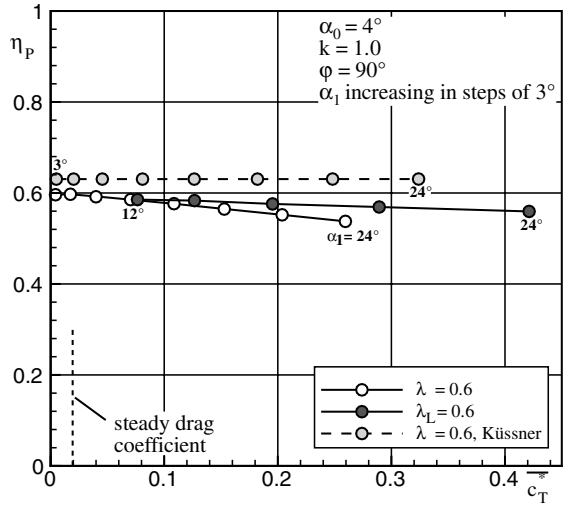

Fig. 23 High thrust and propulsive efficiency for constant amplitude ratios λ_L and λ.

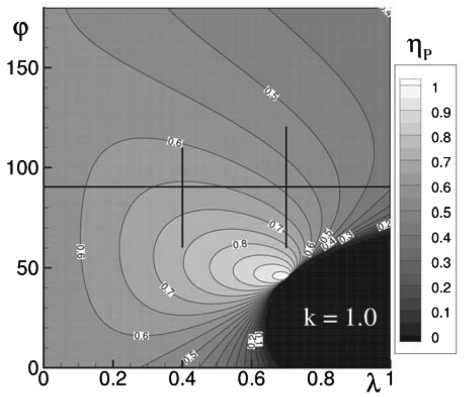

Fig. 24 Propulsive efficiency over motion phase shift φ and amplitude ratio λ for Küssner's theory.

approaching zero. Nevertheless, how thrust and efficiency develop in the viscous case was investigated (see Fig. 25). For $\lambda = 0.4$, an increase in efficiency of up to 9% could have been expected from the Küssner results, but an increase of only 2% is gained. At $\lambda = 0.7$, at least 8% of the expected 18% increase is received. However, the efficiency is not higher than that already gained at $\lambda = 0.4$. The

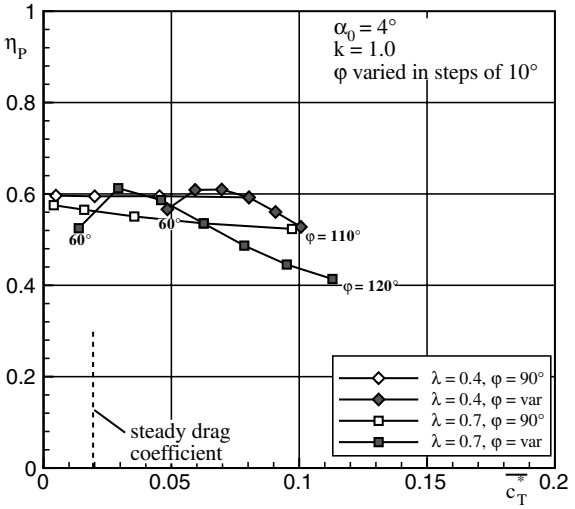

Fig. 25 Thrust and propulsive efficiency for a variation of φ at two fixed amplitude ratios λ.

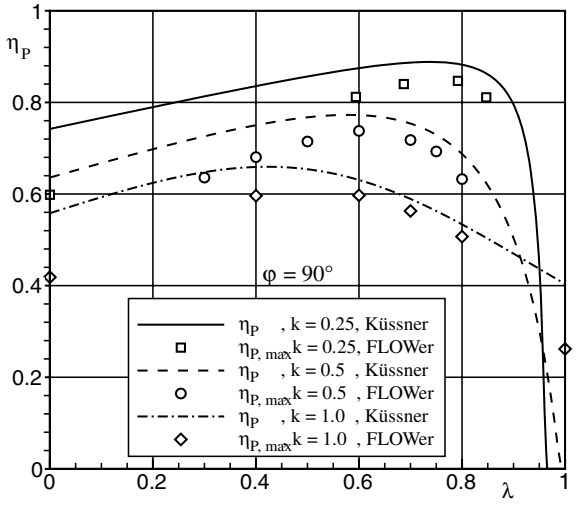

Fig. 26 Overview of calculated maximum propulsive efficiencies compared with Küssner's theory.

decrease of thrust with decreasing phase shift might be problematic if one wants to make use of an improved efficiency. However, the phase shift may as well be exploited as an additional way to control thrust at high reduced frequencies, without the need to change the motion amplitudes.

4. *Overview over the Calculated Propulsive Efficiencies*

For the three reduced frequencies of $k = 0.25$, 0.5, and 1, the maximum efficiencies calculated with FLOWer are compared with the Küssner [14] results in Fig. 26. To visualize a realistic minimum drag loss, only cases were considered in which at least the steady-state drag is overcome. The shapes of the efficiency curves from Küssner's theory are well matched for $k = 0.25$ and 0.5, with good agreement between the amplitude ratios needed for best efficiencies. For $k = 1.0$, a slight shift between the curves is found, with higher λ performing better than expected from the Küssner results. For deviations from the optimal λ, the drag losses are increasing for all frequencies. For the pure plunge motion with $\lambda = 0$, not only the vortex losses are large, but so are the drag losses. Obviously, the pure plunge motion is not well suited to obtain high efficiencies.

V. Conclusions

For all reduced frequencies investigated and in the range of efficient amplitude ratios, propulsive efficiencies are found to have a nearly constant offset between viscous and inviscid calculations. Because the viscous efficiencies were calculated using the steady airfoil drag as thrust correction, the existence of the offset confirms that Küssner's [14] statement, discussed in Sec. IV.A.1, is valid for the SD7003 airfoil. The mean airfoil drag of the moving airfoil is higher than the airfoil drag at mean angle of attack. A constant offset means that absolute drag losses are increasing with increasing motion amplitudes, but at the same time, input and output power are increasing at the same rate. These results seem to provide an opportunity to apply a simple correction on inviscid analytical solutions. However, it cannot be expected that such a correction would generally work. If an airfoil or mean angle of attack is chosen that does not work well in the steady-flow case, then it can be subject to an unsteady drag reduction, meaning that it can perform more efficiently in the unsteady case. This would result in a variable offset. Also, if the thrust correction value is not chosen carefully for such an airfoil [i.e., just using $c_d(\alpha_0)$], efficiencies of over 100% could be calculated, due to unsteady drag reduction.

Huge differences in the predicted transition location were found between the steady and unsteady transition methods at the high reduced frequency of $k = 1.0$. Although this did not have a noteworthy effect on the calculated force coefficients, it cannot be concluded that unsteady transition prediction is, in general,

unnecessary for these flows. Calculations of airfoils with large adverse LSBs in the low- and medium-angle-of-attack range for stationary onflow might be largely affected by the differences in transition location. For the SD7003 airfoil, the transition location is only relevant closer to the leading edge, where the difference between the two transition-prediction methods diminishes. For low reduced frequencies, steady transition prediction seems to be sufficient.

The importance of an accurate modeling of LSBs for unsteady flows is seen for the validation case III, in which a small change in N_{crit}, and thus the transition location, strongly affects the drag. Simulations assuming purely laminar or fully turbulent flows might give acceptable results for moderate motion amplitudes and angles of attack, but they will most likely fail for cases in which flow separation over the full airfoil surface can be expected.

A general result that can already be concluded from 2D inviscid theory is that the desired thrust is most efficiently produced with motion amplitudes that are as large as possible, giving a reduced frequency that is as small as possible. For an optimized 3D application, this does not necessarily hold true, because unsteady induced drag would have to be taken into account. Also, for the design and optimization of a 3D flapping-wing MAV, other aspects would have to be considered, such as a flight mechanics model incorporating the real nonhorizontal flight path and an aeroelastic approach that considers the flexibility of the wing. The simulation of a flexible moving airfoil and its validation is being investigated in a joint effort [46], which is considered a necessary step to high-quality 3D aeroelastic simulations.

Acknowledgments

The presented investigations were funded by the Deutsche Forschungs-Gemeinschaft. The authors thank G. Schrauf for providing the LILO linear stability solver and M. Neef for implementing Küssner's [14] theory in a verified computer script.

References

[1] Pornsin-Sisirak, T., Tai, Y. C., Ho, C. M., and Keennon, M., "Microbat—A Palm-Sized Electrically Powered Ornithopter," 2001 NASA/JPL Workshop on Biomorphic Robotics, 14–16 Aug. 2000.

[2] Madangopal, R., Kahn, Z. A., and Agrawal, S. K., "Biologically Inspired Design of Small Flapping Wing Air Vehicles Using Four-Bar Mechanisms and Quasi-Steady Aerodynamics," *Journal of Mechanical Design*, Vol. 127, July 2005, pp. 809–816. doi:10.1115/1.1899690

[3] Raney, D. L., and Slominski, E. C., "Mechanization and Control Concepts for Biologically Inspired Micro Air Vehicles," *Journal of Aircraft*, Vol. 41, No. 6, Nov.–Dec. 2004, pp. 1257–1265.

[4] Jones, K. D., and Platzer, M. F., "Experimental Investigation of the Aerodynamic Characteristics of Flapping-Wing Micro Air Vehicles," 41st Aerospace Science Meeting & Exhibit, Reno, NV, AIAA Paper 2003-0418, 6–9 Jan. 2003.

[5] Kellog, J., Foch, R., Cylinder, D., Kahn, A., Ramamurti, R., Sandberg, W., and Srull, D., "Flight Control Mechanisms for Unconventional Micro Air Vehicles," First European Micro Air vehicle Conference and Flight Competition, Braunschweig, Germany, German Inst. of Navigation (DGON), Bonn, Germany, 13–14 July 2004.

[6] Tuncer, I. H., and Platzer, M. F., "Thrust Generation Due to Airfoil Flapping," *AIAA Journal*, Vol. 34, No. 2, Feb. 1996, pp. 324–331.

[7] Jones, K. D., and Platzer, M. F., "Numerical Computation of Flapping-Wing Propulsion and Power Extraction," 35th AIAA Aerospace Sciences Meeting and Exhibit, Reno, NV, AIAA Paper 1997-0826, 6–10 Jan. 1997.

[8] Ramamurti, R., and Sandberg, W. C., "Simulation of Flow About Flapping Airfoils Using Finite Element Incompressible Flow Solver," *AIAA Journal*, Vol. 39, No. 2, Feb. 2001, pp. 253–260.

[9] Neef, M. F., "Analyse des Schlagflugs Durch Numerische Strömungsberechnung," Dissertation, Technical Univ. of Braunschweig, Braunschweig, Germany, 2002, also available online at www.biblio.tu-bs.de/ediss/data/20021021a/20021021a.html.

[10] Jones, K. D., Castro, B. M., Mahmoud, O., Pollard, S. J., Platzer, M. F., Neef, M. F., Gonet, K., and Hummel, D., "A Collaborative Numerical and Experimental Investigation of Flapping-Wing Propulsion," 40th AIAA Aerospace Sciences Meeting and Exhibit, Reno, NV, AIAA Paper 2002-706, 2002.

[11] Windte, J., and Pfingsten, K. C., "On 2D Motion Parameters for Flapping Wing Propulsion," First European Micro Air vehicle Conference and Flight Competition, German Inst. of Navigation (DGON), Bonn, Germany, 13–14 July 2004.

[12] Tuncer, I. H., and Kaya, M., "Optimization of Flapping Airfoils for Maximum Thrust and Propulsive Efficiency," *AIAA Journal*, Vol. 43, No. 11, 2005, pp. 2329–2336.

[13] Anderson, J. M., Streitlien, K., Barret, D. S., and Triantafyllou, M. S., "Oscillating Foils of High Propulsive Efficiency," *Journal of Fluid Mechanics*, Vol. 360, 1998, pp. 41–72. doi:10.1017/S0022112097008392

[14] Küssner, H. G., "Zusammenfassender Bericht über den Instationären Auftrieb von Flügeln," *Luftfahrtforschung*, Vol. 13, 1936, pp. 410–424.

[15] Würz, W., "Hitzdrahtmessungen zum Laminar-Turbulenten Strömungsumschlag in Anliegenden Grenzschichten und Ablöseblasen Sowie Vergleich mit der Laminaren Stabilitätstheorie und Empirischen Umschlagskriterien," Dissertation, Univ. of Stuttgart, Stuttgart, Germany, 1995.

[16] Lang, M., Marxen, O., Rist, U., and Wagner, S., *Experimental and Numerical Investigations on Transition in a Laminar Separation Bubble*, edited by S. Wagner, U. Rist, H. J. Heinemann, and R. Hilbig, Vol. 77, Notes on Numerical Fluid Mechanics and Multidisciplinary Design, Vieweg, Braunschweig, Germany, 2002, pp. 207–214.

[17] Marxen, O., Rist, U., and Wagner, S., "The Effect of Spanwise-Modulated Disturbances on Transition in a 2-D Separated Boundary Layer," AIAA Paper 2003-0789, 2003.

[18] Rist, U., *Instability and Transition Mechanisms in Laminar Separation Bubbles*, von Kármán Inst. Lecture Series, RTO-AVT-VKI-104, von Kármán Inst. for Fluid Dynamics, Rhode-Saint-Genèse, Belgium, 24–28 Nov. 2003.

[19] Radespiel, R., Windte, J., and Scholz, U., "Numerical and Experimental Flow Analysis of Moving Airfoils with Laminar Separation Bubbles," *AIAA Journal*, Vol. 45, No. 6, June 2007, pp. 1346–1356. doi:10.2514/1.25913

[20] "Experimental and Computational Investigations in Low Reynolds Number Aerodynamics, with Applications to Micro Air Vehicles (MAVs)," NATO Research and Technology Organisation Rept. RTO-TR-AVT-101, Neuilly-sur-Seine, France, June 2007.

[21] Van Ingen, J. L., "A Suggested Semi-Empirical Method for the Calculation of the Boundary Layer Transition Region," Delft Univ. of Technology, Rept. VTH-74, Delft, Holland, The Netherlands, 1956.

[22] Kroll, N., Rossow, C. C., Schwamborn, D., Becker, K., and Heller, G., "MEGAFLOW—A Numerical Flow Simulation Tool for Transport Aircraft Design," International Council of the Aeronautical Sciences Paper 1105, 2002.

[23] Schrauf, G., "LILO 2.1 User's Guide and Tutorial," G. Schrauf, Bremen, Germany, 2006.

[24] Schrauf, G., "An Inverse Rayleigh Iteration for Complex Band Matrices," *ACM Transactions on Mathematical Software*, Vol. 17, No. 1, 1991, pp. 335–340.

[25] Schrauf, G., "Transition Prediction Using Different Linear Stability Analysis Strategies," AIAA Paper 94-1848-CP, 1994.

[26] Gaster, M., "A Note on a Relation between Temporally Increasing and Spatially Increasing Disturbances in Hydrodynamic Stability," *Journal of Fluid Mechanics*, Vol. 14, 1962, pp. 222–224. doi:10.1017/S0022112062001184

[27] Gazaix, M., Jollès, A., and Lazareff, M., "The elsA Object-Oriented Computational Tool for Industrial Applications," ICAS 2002 Congress, Toronto, Canada, International Council of the Aeronautical Sciences Paper 2002-1.10.3, 8–13 Sept. 2002.

[28] Birnbaum, W., "Das Ebene Problem des Schlagenden Flügels," Dissertation, Univ. of Göttingen, Göttingen, Germany, 1922.

[29] Küssner, H. G., "Schwingungen von Flugzeugflügeln," *Luftfahrtforschung*, Vol. 4, 1929, pp. 41–62.

[30] Theodorson, T., "General Theory of Aerodynamic Instability and the Mechanism of Flutter," NACA Rept. 496, 1934.

[31] Lilienthal, O., *Der Vogelflug als Grundlage der Fliegekunst*, R. Gärtners Verlagsbuchhandlung, Berlin, 1889.

[32] Windte, J., Scholz, U., and Radespiel, R., "Validation of the RANS-Simulation of Laminar Separation Bubbles on Airfoils," *Aerospace Science and Technology*, Vol. 10, No. 6, 2006, pp. 484–494. doi:10.1016/j.ast.2006.03.008

[33] Yuan, W., Khalid, M., Windte, J., Scholz, U., and Radespiel, R., "Computational and Experimental Investigations of Low-Reynolds-Number Flows Past an Aerofoil," *The Aeronautical Journal*, Vol. 111, No. 1115, Jan. 2007, pp. 17–29.

[34] Ol, M., McAuliffe, B. R., Hanff, E. S., Scholz, U., and Kaehler, Ch.,

"Comparison of Laminar Separation Bubble Measurements on a Low Reynolds Number Airfoil in Three Facilities," AIAA Paper 2005-5149, 2005.

[35] Hain, R., and Kaehler, C. J., "Advanced Evaluation of Time-Resolved PIV Image Sequences," 6th International Symposium on Particle Image Velocimetry, Pasadena, CA, California Inst. of Technology Paper S01-5, 21–23 Sept. 2005.

[36] Watmuff, J. H., "Evolution of a Wave Packet into Vortex Loops in a Laminar Separation Bubble," *Journal of Fluid Mechanics*, Vol. 397, 1999, pp. 119–169. doi:10.1017/S0022112099006138

[37] Muti Lin, J. C., and Pauley, L. L., "Low-Reynolds-Number Separation on an Airfoil," *AIAA Journal*, Vol. 34, No. 8, Aug. 1996, pp. 1570–1577.

[38] Tatineni, M., and Zhong, X., "Numerical Simulation of Unsteady Low-Reynolds-Number Separated Flows over Airfoils," 28th AIAA Fluid Dynamics Conference, AIAA Paper 1997-1929, 1997.

[39] Selig, M. S., Donovan, J. F., and Fraser, D. B., "Airfoils at Low Speeds," *Soar Tech*, Herk Stokely, Virginia Beach, VA, 1989.

[40] Selig, M. S., Guglielmo, J. J., Broeren, A. P., and Giguère, P., "Summary of Low-Speed Airfoil Data," *Soar Tech*, Vol. 1, Herk Stokely, Virginia Beach, VA, 1995.

[41] Selig, M. S., Lyon, C. A., Giguère, P., Ninham, C. P., and Guglielmo, J. J., "Summary of Low-Speed Airfoil Data," *Soar Tech*, Vol. 2, Herk Stokely, Virginia Beach, VA, 1996.

[42] Selig, M. S., Lyon, C. A., Broeren, A. P., Giguère, P., Gopalarathman, A., and Selig, M. S., "Summary of Low-Speed Airfoil Data," *Soar Tech*, Vol. 3, Herk Stokely, Virginia Beach, VA, 1997.

[43] Guglielmo, J. J., and Selig, M. S., "Spanwise Variations in Profile Drag for Airfoils at Low Reynolds Numbers," *Journal of Aircraft*, Vol. 33, No. 4, July–Aug. 1996, pp. 699–707.

[44] Menter, F. R., "Two-Equation Eddy-Viscosity Transport Turbulence Model for Engineering Applications," *AIAA Journal*, Vol. 32, No. 8, 1994, pp. 1598–1605.

[45] Ewald, B. F. R., "Wind Tunnel Wall Corrections," AGARD Rept. AGARD-AG-336, Paris, 1998, pp. 2–14.

[46] Unger, R., Kleinert, J., Haupt, M. C., Horst, P., Windte, J., Bansmer, S., Kähler, C. J., and Radespiel, R., "Design and Analysis of an Aeroelastic Validation Experiment for Moving Flexible Airfoils," 1st CEAS European Air and Space Conference, Berlin, Confederation of European Aerospace Societies Paper 2007-014, Sept. 2007.

G. Abate
Guest Editor